High energy density in 2D/3D/2D heterostructures that combine low relaxation time and low energy loss

Sangmoon Han[1]†, Justin S. Kim[1,2]†, Eugene Park[3]†, Yuan Meng[1], Zhihao Xu[1,2], Alexandre C. Foucher[3], Gwan Yeong Jung[1,2], Ilpyo Roh[1,4], Sangho Lee[5], Sun Ok Kim[1,6], Ji-Yun Moon[1], Seung-Il Kim[1], Sanggeun Bae[1,2], Xinyuan Zhang[3], Bo-In Park[5], Seunghwan Seo[5,7], Yimeng Li[1], Heechang Shin[8], Kate Reidy[3], Anh Tuan Hoang[8], Suresh Sundaram[9], Phuong Vuong[9], Chansoo Kim[2,10], Junyi Zhao[2,10], Jinyeon Hwang[11], Chuan Wang[2,10], Hyungil Choi[4], Dong-Hwan Kim[6,12], Jimin Kwon[13], Jin-Hong Park[7], Abdallah Ougazzaden[9,14], Jae-Hyun Lee[15], Jong-Hyun Ahn[8], Jeehwan Kim[3,5], Rohan Mishra[1,2], Hyung-Seok Kim[11,16], Frances M. Ross[3]*, and Sang-Hoon Bae[1,2]*

[1]Deapartment of Mechanical Engineering and Materials Science, Washington University in St. Louis, Saint Louis, MO, 63130, USA

[2]The Institution of Materials Science and Engineering, Washington University in St. Louis, Saint Louis, MO, 63130, USA

[3]Department of Materials Science and Engineering, Massachusetts Institute of Technology, Cambridge, MA, 02139, USA

[4]M.O.P. materials, Seoul 07285, Republic of Korea

[5]Department of Mechanical Engineering, Massachusetts Institute of Technology, Cambridge, MA, 02139 USA

[6]Precision Biology Research Center, Sungkyunkwan University, Suwon 16419, Republic of Korea

[7]Department of Electrical and Computer Engineering, Sungkyunkwan University, Suwon 16419, Republic of Korea

[8]School of Electrical & Electronic Engineering, Yonsei University, Seoul, Republic of Korea

[9]CNRS, Georgia Tech – CNRS IRL 2958, GT-Europe, Metz, France.

[10]Department of Electrical and System Engineering, Washington University in St. Louis, Saint Louis, MO, 63130, USA

[11]Energy Storage Research Center, Korea Institute of Science and Technology, Seoul 02792, Republic of Korea

[12]School of Chemical Engineering, Sungkyunkwan University, Suwon 16419, Republic of Korea

[13] Department of Electrical Engineering, Ulsan National Institute of Science and Technology (UNIST), Ulsan 44919, Republic of Korea

[14]School of Electrical and Computer Engineering, Georgia Institute of Technology, Atlanta, GA 30332-0250, USA

[15]Department of Materials Science and Engineering and Department of Energy Systems Research, Ajou University, Suwon 443-749, Republic of Korea

[16]KHU-KIST Department of Converging Science and Technology, Kyung Hee University, Seoul 02447, Republic of Korea

*Corresponding author. Email: fmross@mit.edu (F. M. R.) sbae22@wustl.edu (S.-H. B.)

†These authors contributed equally to this work.

Abstract

Electrostatic capacitors are foundational components in advanced electronics and high-power electrical systems due to their ultrafast charging/discharging capability. Ferroelectric materials offer high maximum polarization, but high remnant polarization has hindered their effective deployment in energy storage applications. Previous methodologies have encountered problems due to the deteriorated crystallinity of the ferroelectric materials. We introduce an approach to control the relaxation time using 2D materials while minimizing energy loss by 2D/3D/2D heterostructures, while preserving the crystallinity of ferroelectric 3D materials. This approach has led to the achievement of an energy density of 191.7 J/cm^3 with an efficiency over 90%. This precise control over relaxation time holds promise for a wide array of applications and has the potential to accelerate the development of highly efficient energy storage systems.

Managing high energy density has become increasingly important in applications ranging from electric power systems to portable electronic devices (*1-3*). Electrostatic capacitors have been widely used for high-energy storage and release due to their ultrafast charge and discharge rate, but their performance is limited by the low maximum polarization (P_m) of conventional dielectric materials (*4, 5*). In contrast, ferroelectric materials such as HfO_2, ZrO_2, and $BaTiO_3$ (BTO) can achieve higher maximum polarization due to their higher electric susceptibilities related to dielectric constants (*6, 7*). However, their high remnant polarization (P_r) limits the effectiveness of energy storage and release during the discharging process (*8*). To overcome this limitation, relaxor-ferroelectric materials have been studied for their ability to achieve high energy densities with low remnant polarization. Through compositional and defect design, nanodomains have been introduced into ferroelectric materials to realize relaxor ferroelectricity, offering a potential avenue for developing high-performance electrostatic capacitors (*9, 10*). These methodologies lead to a redistribution of domain walls that can serve as effective relaxor-like defects to suppress the formation of large polar domains and reduce the remnant polarization. Although recent advances have shown great promise in realizing relaxor ferroelectricity by inducing nanodomains in ferroelectric materials through composition and defect engineering, these approaches result in the loss of crystallinity, leading to reduced permittivity and sacrificing the maximum polarization. Moreover, some approaches have shown a restriction in achieving a high polarization saturation limit, resulting in polarization saturation at a low electric field and leading to low energy density (U_e), despite substantial breakthrough otherwise (*11*). These limitations highlight the need for a different approach that can supplement previous methods and lead to the development of electrostatic capacitors with extremely high energy density.

We introduce a strategy for precise control of the relaxation time of polarization that maintains minimal energy loss by using monolayer 2D materials produced by the layer splitting technique (*12*). We achieve this by using artificially designed 2D/single-crystalline 3D/2D (2D/C-3D/2D) heterostructures. We use a layer transfer technique to produce freestanding single-crystalline $BaTiO_3$ (C-BTO) where both interfaces can be manipulated, and we form 2D/C-3D/2D heterostructures by addition of various 2D materials. Unlike previous approaches that deteriorate ferroelectric materials by involving structural changes, our approach preserves the single-crystal nature of the BTO. Instead, we sandwich a C-BTO layer with 2D materials in the form of a freestanding membrane, such that the Maxwell-Wagner (MW) effect, a relaxation by charge

accumulation at heterogeneous interfaces (*13, 14*), takes place at the interfaces to change the relaxation time. Thickness control of 2D materials with atomic precision by the layer-resolved splitting technique (*15, 16*) enables minimal energy loss and tangent delta (tan δ), a dielectric loss due to electrical phase difference (*12, 17*), while controlling relaxation time. Using this strategy, we can effectively suppress the remnant polarization of ferroelectric materials while maintaining the maximum polarization. We show this allows for an energy density of 191.7 J/cm^3 with an efficiency of over 90%. We believe our approach has the potential to enhance the performance of dielectric materials and other related applications that require high-energy storage systems.

MW relaxation at 2D/3D interfaces

The Miller model inspired by classic Debye relaxation provides a theoretical framework for controlling spontaneous polarization by manipulating the relaxation time (Fig. 1A). One approach for regulating the relaxation time involves the creation of heterostructures comprising two distinct materials, typically a ferroelectric material and a dielectric material, due to their disparities in electrical conductivity and permittivity (*18*). These heterostructures enable the accumulation of charge at the interfaces between the phases when subjected to an alternating electric field, a phenomenon known as the MW relaxation effect. This effect offers a means to influence and modulate the relaxation time within the heterostructures. However, effective modulation of the relaxation time has been difficult while conserving maximum polarization in conventional heterostructures through the MW effect for two reasons: (i) Previous attempts mainly led to the deterioration of ferroelectricity, generating strain or creating multi-domain structures by the additional layers forming chemical bonds with the ferroelectric material (*19, 20*). (ii) As the thickness increases due to the additional layers needed for the MW effect, this inevitably leads to additional energy loss and higher tan δ, which is closely associated with dielectric loss (*21-23*). We circumvent these problems through the use of 2D/C-3D/2D heterostructures, formed using a layer transfer technique (*24-26*). We first produce freestanding C-BTO of 30 nm thickness. The film is sufficiently high quality that we observed only the (001) orientation in electron back-scattering diffraction mapping. We use a variety of characterization techniques to show the C-BTO quality (Fig. S1-S4). A schematic representation of the 2D/C-BTO/2D fabrication process is shown in Fig. S5. The freestanding nature of these C-BTO nanomembranes then allows us to coat both sides with other materials to produce artificial heterostructures.

We anticipated that the choice of 2D materials for the coating layer will induce an efficient MW

effect while avoiding substantial energy loss, because of both the atomically thin nature of the 2D layers and the lack of strong chemical bonding at the heterointerfaces. To aid in 2D materials choice, we show a summary of the conductivity *vs.* dielectric constant of representative 2D materials (Fig. 1B) (*27-33*). The higher the dielectric constant and the lower the conductivity, the stronger MW relaxation induced at the interface. From the 2D candidates, we choose graphene (a 2D semimetal), MoS_2 (a 2D semiconductor), and *h*-BN (a 2D insulator). Although some studies of MoS_2 have shown ferroelectricity due to structural deformation, our previous measurements (*12*) of devices that included similar MoS_2 did not show such behavior, so we do not expect or include any ferroelectric behavior of the MoS_2 layer in our analysis. Selecting these materials is because we anticipate the possibility of observing diverse variations in relaxation time and tan δ within different artificial heterostructures. For comparison purposes, we also fabricated two different heterostructures of 3 nm Al_2O_3/C-BTO/Al_2O_3. One heterostructure was formed by atomic layer deposition, for which we anticipate strong chemically bonded BTO/Al_2O_3 interfaces (Fig. S6). We formed the other heterostructure by layer transfer without an annealing process that we anticipated lacking strong chemically bonded interfaces (Fig. S7).

After fabrication of this set of heterostructures, we measured the dielectric Cole-Cole plot at the frequency range 10^2 - 10^6 Hz (Fig. 1C) and calculated the relaxation times at 10 kHz (Fig. S8) (*31, 32*). In the bare freestanding C-BTO nanomembranes, we obtained a value of ~0.09 for $\omega\tau$, which is defined as the product of angular frequency (ω) of 10 kHz and relaxation time (τ). We calculated the $\omega\tau$ values of Al_2O_3/C-BTO/Al_2O_3 samples to be 0.95 and 16.4 for the strongly bonded and weakly bonded samples, respectively. We expect that some internal strain in the Al_2O_3 and C-BTO may be present, due to the difference in thermal expansion coefficients, and any such effects are included in the relaxation times. This result indicates that the weakly bonded and discontinuous interface provides a higher relaxation time than that of a strongly chemically bonded interface (*36, 37*). However, we measured the tan δ values of the strongly and weakly bonded Al_2O_3/C-BTO/Al_2O_3 to be 7.4 x 10^{-3} and 31.0 x 10^{-3} at 10 kHz, which are much higher than those of bare C-BTO (Fig. 1D). We expect substantial energy loss and decrease in the maximum polarization density based on these values (*21, 38, 39*). In contrast, the heterostructures we fabricated using layer-resolved splitting of 2D materials, enabling thickness control of 2D materials at atomic precision (*15, 26*), yielded lower tan δ and $\omega\tau$ values. One monolayer *h*-BN (1ML-*h*-BN)/C-BTO/1ML-*h*-BN had a $\omega\tau$ = 9.5 and tan δ = 3.7 x 10^{-3} at 10 kHz. More effective control of

relaxation time is clearly achievable using *h*-BN compared to conventional dielectric materials such as Al_2O_3. Additionally, the lower tan δ with *h*-BN suggests the potential for relatively smaller energy loss using 2D materials. We attribute the benefits of the 2D material to be its atomic thickness, compared to the relatively large Al_2O_3 layer thickness. To further explore our hypothesis, we repeated the experiment by creating an artificial heterostructure using MoS_2, known for its lower carrier density and dielectric constant, as well as graphene, which exhibits much lower values. The one monolayer MoS_2 (1ML-MoS_2)/C-BTO/1ML-MoS_2 heterostructure had a $\omega\tau$ value of 1.2 and a tan δ of 1.61 x 10^{-3}, while the one monolayer graphene (1ML-Gr)/C-BTO/1ML-Gr heterostructure had a $\omega\tau$ value of 0.2 and an even lower tan δ of 7.6 x 10^{-5}. Unlike the 1ML-*h*-BN/C-BTO/1ML-*h*-BN heterostructure, which displayed two distinct peaks indicating the presence of MW relaxation (*40, 41*), the 1ML-MoS_2/C-BTO/1ML-MoS_2 heterostructure did not exhibit clear peak separation, instead displaying an asymmetric Gaussian distribution. This still proves the presence of MW relaxation. However, the 1ML-Gr/C-BTO/1ML-Gr heterostructure did not show similar behavior in the tan δ measurement despite its extremely low tan δ. These findings highlight the role of the 2D materials in influencing and modulating relaxation time and tan δ within the heterostructures.

Polarization of artificial heterostructures

We expect the large $\omega\tau$ values caused by the large relaxation time induce a strong reduction in the remnant polarization. We measured the polarization-electric field (*P*-*E*) loop of the unmodified C-BTO and the strongly and weakly chemically bonded Al_2O_3/C-BTO/Al_2O_3 heterostructures, all at 10 kHz (Fig. 2A-B). 30-nm thick BTO was chosen because it has higher P_m, lower P_r, and lower electrical leakage than other thicknesses tested (Fig. S9). The maximum polarizations of both Al_2O_3/C-BTO/Al_2O_3 samples were dramatically decreased because of the tan δ. However, the remnant polarization of the strongly bonded sample is much higher than the weakly bonded sample. These results agree with our expectation, driven by the tan δ and relaxation time values. Nevertheless, the Al_2O_3/C-BTO/Al_2O_3 with weakly bonded interfaces still provide low maximum polarization and thus poor energy storage performance, because of the high tan δ attributed to the thick nature of Al_2O_3.

Based on our understanding that relaxation time can be effectively controlled while minimizing tan δ, we conducted *P*-*E* loop measurements on the various 2D/C-BTO/2D heterostructures (Fig. 2C). First, we examined *h*-BN/C-BTO/*h*-BN structures and observed a reduction in remnant

polarization. However, this reduction also led to a decrease in maximum polarization, resulting in a notable decline in energy storage density and efficiency. To mitigate the decrease in maximum polarization, we employed MoS_2, which possesses a higher conductivity than *h*-BN and is thus expected to minimize the MW relaxation. Indeed, when C-BTO was coated with 1ML-MoS_2, we observed a smaller decrease in maximum polarization. However, we also noted an insufficient decrease in remnant polarization, leading to energy loss. This insufficient decrease is attributed to the increase in conductivity of 1ML-MoS_2, in which we confirmed the Fermi level shift due to the metal contact through density functional theory calculations (Fig. S10). Meanwhile, the successful suppression of the remnant polarization is observed in heterostructures using bilayer (2ML)-MoS_2, formed by sequentially transferring 1ML-MoS_2 twice, and C-BTO. We propose that the free electrons of the electrodes do not affect the MoS_2 layer adjacent to the C-BTO, providing a sufficiently low conductivity to allow for screening of the dielectric polarization (Fig. S11). We further investigated heterostructures containing graphene, which has a smaller dielectric constant. However, due to its high charge density, we were unable to induce an effective relaxation time delay. Instead, the *P*-*E* loop slightly decreased because of the small increase in the dielectric loss at the non-chemically bonded interface of the graphene/C-BTO (*42*). We attribute such performance, with small remnant polarization and high maximum polarization, to several factors: (i) The artificial heterostructures do not sacrifice the crystallinity of single crystalline ferroelectric materials, unlike conventional heterostructures that experience lattice and thermal mismatch issues. (ii) The atomically thin 2D layers provide extremely low tan δ, preventing a high dielectric loss and decrease in the dielectric constant. (iii) The weakly bonded interface facilitates a substantial increase in dielectric relaxation even when the layer is atomically thin, effectively decreasing the remnant polarization. Together, we expect the small remnant polarization and large maximum polarization to lead to high energy density and high efficiency. To analyze which of the artificial heterostructures are most suitable for high energy density (Fig. 2D-E), we subtract the maximum polarization from the remnant polarization ($P_m - P_r$) - related to the energy density - and divide the maximum polarization by the remnant polarization (P_m/P_r) - related to the efficiency, according to the $\omega\tau$. Up to a $\omega\tau$ value of 3.4, the $P_m - P_r$ and P_m/P_r values increased, indicating improved energy density and efficiency. For $\omega\tau > 3.4$, even though P_m/P_r increased, $P_m - P_r$ rapidly decreased. Considering these results, we therefore anticipate that the 2D/C-BTO/2D heterostructures with $\omega\tau$ around 3.4 (1ML-MoS_2/C-BTO/1ML-MoS_2 and 2ML-MoS_2/C-BTO/2ML-MoS_2) provide the

largest energy storage system in our samples (Cole-Cole plot of 2ML-MoS_2/C-BTO/2ML-MoS_2; Fig. S12)

Atomic scale polarization distribution

To gain a more comprehensive understanding of polarization behavior in the artificially designed 2D/C-3D/2D structures, we conducted additional electrical measurements and obtained atomic-scale structural information for the most effective structure, MoS_2/C-BTO/MoS_2. Fig. 3A shows high-angle annular dark field (HAADF) and integrated differential phase contrast (iDPC) images of this sample measured by scanning transmission electron microscopy (STEM). We characterized the sample after hysteresis tests for 10 cycles under an electric field of -5 to 5 MV/cm at 10 kHz. We measured the lattice spacings of the C-BTO in all samples to be about 0.409 nm, corresponding to the (001) lattice plane of the BTO perovskite structure and indicating preferred growth along the [001] direction. Our HAADF and iDPC images clearly show the gap between the lattice structures of the 2ML-MoS_2 and C-BTO and some interfacial roughness (further example images are shown in Fig. S13). Thus, structural discontinuity at the top and bottom surfaces of the C-BTO can work as a screener for dielectric polarization in the C-BTO crystal (*43, 44*), leading to a relatively small remnant polarization. To further confirm the role of the 2D layer, we measured the *P-E* curve after mechanically exfoliating both the top and bottom MoS_2 layers from the 2ML-MoS_2/C-BTO/2ML-MoS_2 heterostructure. The hysteresis after removing the MoS_2 layers is similar to that of bare C-BTO (see the comparison in Fig. 3B), indicating that the pseudo-relaxor ferroelectric behavior exhibited by the 2D/3D/2D heterostructure is driven by charge compensation rather than relaxor ferroelectricity, and that the 2D layers did not directly affect the dipoles inside the C-BTO crystal, preserving the high polarization.

Another intriguing aspect of our artificial 2D/3D/2D heterostructure is the observation that as the DC electric field increases, the polarization correspondingly increases, with the maximum polarization approaching that of C-BTO. This phenomenon indicates a strong correlation between the applied electric field and the relaxation time within the artificial heterostructure. We show the dielectric Cole-Cole plots of the C-BTO and 2ML-MoS_2/C-BTO/2ML-MoS_2 samples at a DC electric field of 0 - 5 MV/cm (Fig. 3C-D), where the frequency-dependent dielectric constants are described in Fig. S14. In the C-BTO sample, the $\omega\tau$ measured at 10 kHz is observed at the right

side of the center of the semicircle regardless of the electric field. In contrast, the $\omega\tau$ of 2ML-MoS_2/C-BTO/2ML-MoS_2 measured at 10 kHz were shifted to the right with increased field, indicating the increase in the relaxation time. We summarize the $\omega\tau$ calculated from dielectric Cole-Cole plot as a function of electric field for the C-BTO, 1ML-MoS_2/C-BTO/1ML-MoS_2, and 2ML-MoS_2/C-BTO/2ML-MoS_2 samples in Fig. 3E. The DC field-dependent Cole-Cole plot of MoS_2/C-BTO/MoS_2 is described in Fig. S15. With increasing field, the relaxation times of the 2D/C-3D/2D become similar to that of the bare C-BTO. We attribute this result to the decrease in the accumulated charge by MW relaxation due to the electric field. This interplay between the electric field and relaxation time provides useful insights into the ferroelectric properties of the artificial 2D/3D/2D heterostructures.

Performance MoS_2/C-BTO/MoS_2

To investigate the complete energy storage performance of the C-BTO and MoS_2/C-BTO/MoS_2 heterostructures, we measured their statistical breakdown strengths (E_b) via Weibull distribution fitting (Fig. 4A and Fig. S16). We calculated the E_b values of the MoS_2/C-BTO/MoS_2 structures to be 5.62 and 5.61 MV/cm, which are comparable with that of C-BTO (5.81 MV/cm) due to the low thicknesses of the C-BTO. Furthermore, our result is consistent with the negligible effective permittivity change arising from the atomically thin 2D layers (*1*). We observed non-zero leakage currents in the C-BTO and MoS_2/C-BTO/MoS_2 heterostructures (Fig. S17), attributed to the narrow band gap nature of BTO and probability of oxygen vacancies (*45, 46*). Nevertheless, the leakage current values are comparable to that of previously reported capacitors with high energy capability (*3, 10, 11*), indicating high reliability and E_b under high electric field conditions. We further calculated from the *P-E* loops at 10 kHz the U_e and efficiencies of the samples at an electric field of ~ 5.6 MV/cm (close to their E_b) (Fig. 4B). As expected, we obtained a higher energy density from the 2ML-MoS_2/C-BTO/2ML-MoS_2 samples (191.7 J/cm^3) than those of the C-BTO (96.9 J/cm^3) and 1ML-MoS_2/C-BTO/1ML-MoS_2 (152.4 J/cm^3) samples. The energy density we observed in the 2ML-MoS_2/C-BTO/2ML-MoS_2 heterostructure exhibits a high value (Fig. S18). These ultrahigh U_e values are the combined results of high polarization density, low hysteresis, and high efficiency (over 90%). The high efficiency is critical to address the energy dissipation of dielectrics for high-power applications, facilitating reliable operation. At higher frequency, smaller P_m and P_r were observed because there is insufficient time to align the dipoles at the higher frequency (Fig. S19). Nevertheless, high energy storage performance is still achieved. We also

conducted stability and reliability tests, crucial for electrostatic energy storage. For a thermal stability test, we measured the *P-E* loops of the MoS_2/C-BTO/MoS_2 structures, which showed good stability of the polarization (Fig. S20) and energy storage performance (Fig. 4C) under a wide temperature range (250 to 400 K) with a small degradation in U_e (< 6%) and efficiency (< 6%). We attribute this U_e and efficiency reduction to the complex thermal scattering of charges accumulated at the non-chemically bonded interfaces (*47*). Nevertheless, the degradation rates are similar to previously reported results, indicating good thermal stability (*9, 48, 49*). During an accelerated charge-and-discharge test shown in Fig. 4D-F, they survived over 10^8 cycles. Moreover, the degradation rate of 2ML-MoS_2/C-BTO/2ML-MoS_2 is < 5% after 10^8 cycles, indicating that our samples are stable during the cycling test. To assess the practical feasibility of our approach, we fabricated a 2ML-MoS_2/C-BTO/2ML-MoS_2 array (Fig. S21). The average P_m has 36.3 ± 9.3 μC/cm^2 at 2.7 MV/cm with suppressed P_r, indicating the potential for practical application.

In conclusion, our findings highlight the complex interplay between different materials in artificially designed 2D/C-3D/2D heterostructures and their impact on remnant polarization, maximum polarization, energy loss, and efficiency. These insights contribute to the understanding of how to optimize the design and performance of high-energy electrostatic capacitors using ferroelectric materials. By utilizing this approach, we anticipate that future advances in the development of more efficient and giant energy storage systems can be achieved.

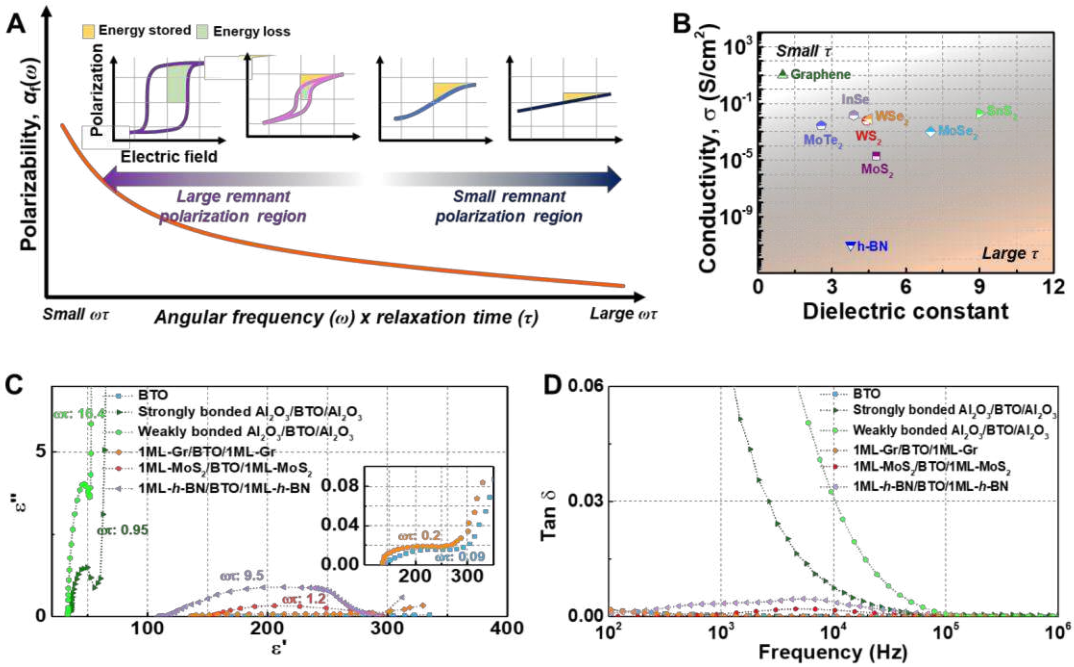

Fig. 1. Management of spontaneous polarization via Miller model inspired from classic Debye relaxation. (**A**) Polarizability *vs.* $\omega\tau$ curve of the Miller model. (**B**) Summary of the conductivity *vs.* dielectric constant curve of several 2D materials. (**C**) Dielectric Cole-Cole plots and (**D**) Tan δ *vs.* frequency curves of the C-BTO, 2D/C-3D/2D, and 3D/C-3D/3D structures.

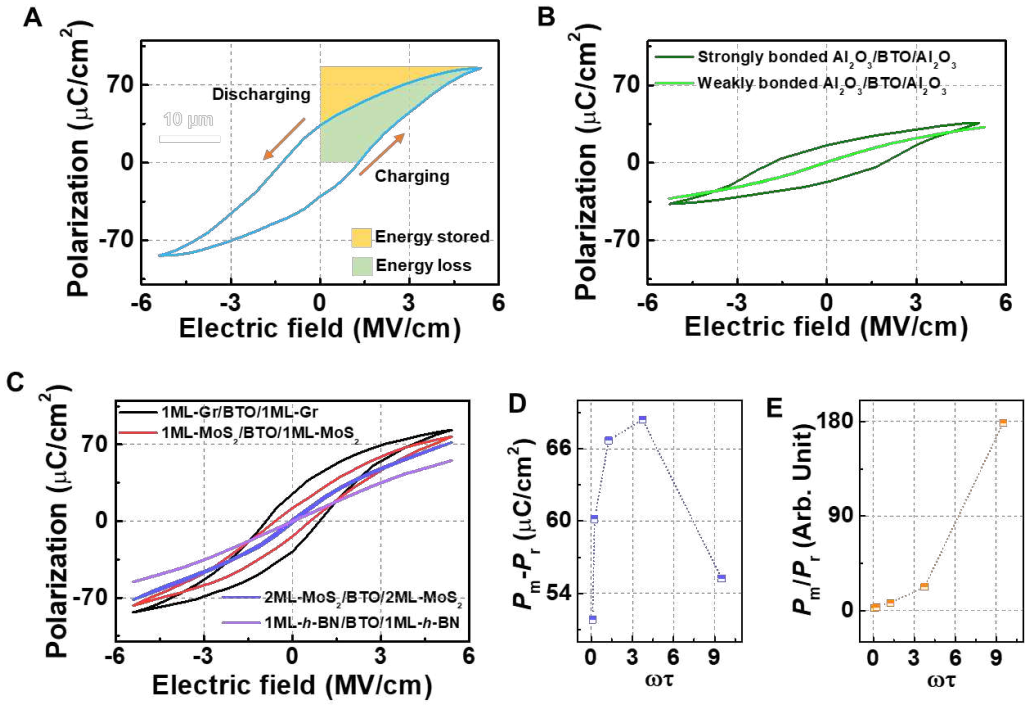

Fig. 2. Polarization of the C-BTO, 3D/3D/3D, and 2D/3D/2D heterostructures. (**A**) *P–E* loop of C-BTO, (**B**) Comparison of *P–E* loops of Al_2O_3/C-BTO/Al_2O_3 with strongly and weakly bonded interfaces. (**C**) *P-E* loop of the 2D/3D/2D heterostructure. The *P–E* loops were measured at 10 kHz. (**D**) $P_m - P_r$ and (**E**) P_m/P_r calculated from the P–E loops.

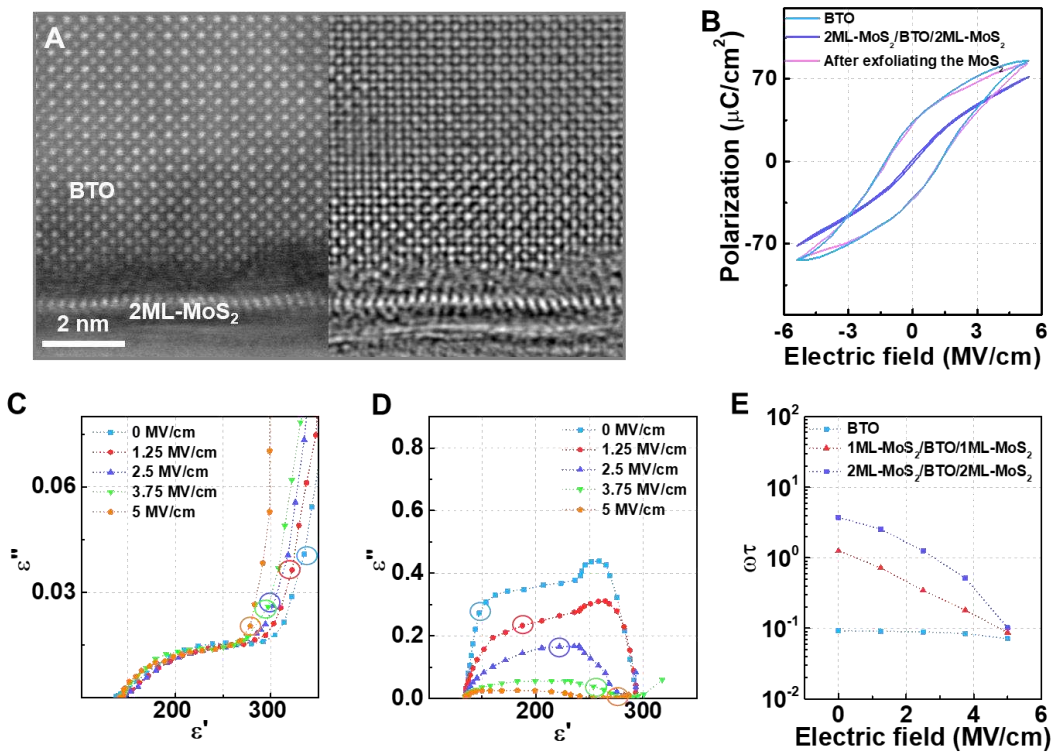

Fig. 3. Atomic-scale polarization distribution and additional electrical performance under bias. (**A**) STEM-HAADF and iDPC images of 2ML-MoS_2/C-BTO/2ML-MoS_2. Separation between the MoS_2 and BTO and interface roughness of the BTO are visible. (**B**) *P-E* loop of the C-BTO, 2ML-MoS_2/C-BTO/2ML-MoS_2, and 2ML-MoS_2/C-BTO/2ML-MoS_2 after mechanically exfoliating the MoS_2 layers. Dielectric Cole-Cole plots of (**C**) C-BTO and (**D**) 2ML-MoS_2/C-BTO/2ML-MoS_2 under DC bias from 0 to 5 MV/cm. (**E**) The $\omega\tau$ under electric field of C-BTO, 1ML-MoS_2/C-BTO/1ML-MoS_2, and 2ML-MoS_2/C-BTO/2ML-MoS_2.

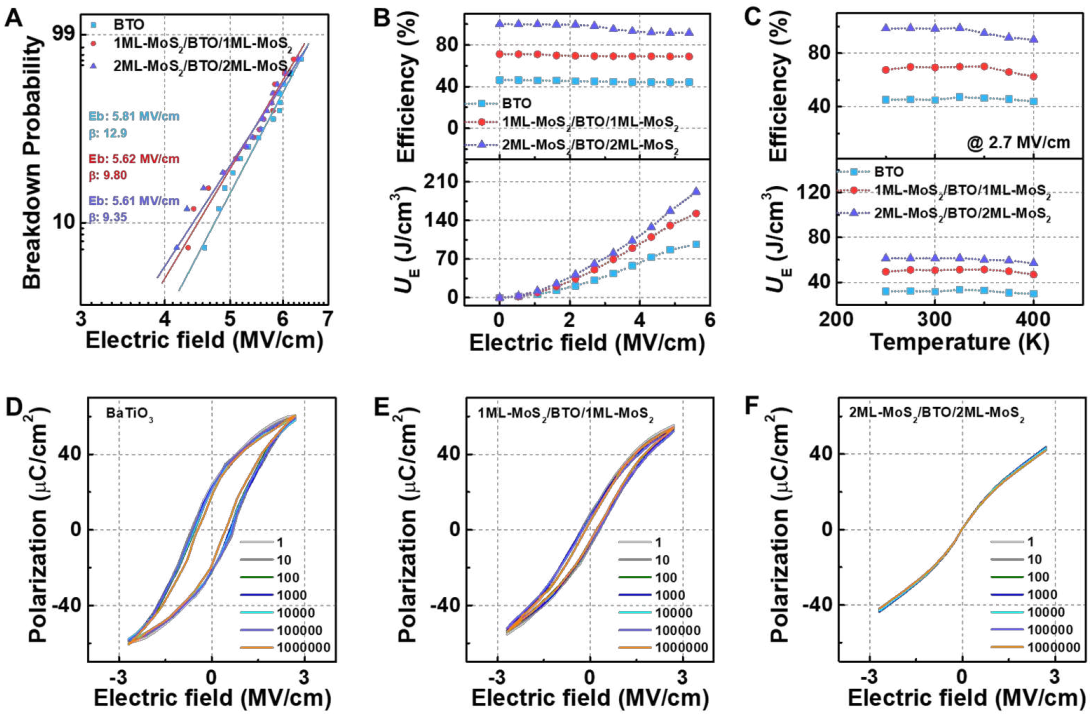

Fig. 4. Energy storage performance of C-BTO and MoS_2/C-BTO/MoS_2 with respect to the number of MoS_2 layers. (**A**) Two-parameter Weibull distribution analysis of the characteristic breakdown fields and (**B**) Voltage-dependent energy density and efficiency of the C-BTO and MoS_2/C-BTO/MoS_2 heterostructures. (**C**) Temperature-dependence of energy densities and efficiencies at the temperature range from 250 to 400K. *P-E* loops of (**D**) C-BTO, (**E**) 1ML-MoS_2/C-BTO/1ML-MoS_2, and (**F**) 2ML-MoS_2/C-BTO/2ML-MoS_2 at temperatures ranging from 250 to 400K.

Supplementary information

Materials and Methods

Single-crystalline $BaTiO_3$ (BTO) growth

Before the growth of the single-crystalline BTO, the native oxide on the $SrTiO_3$(100) (STO) substrate with a size of 10 x 10 x 0.5 mm was removed by chemical wet etching into buffered oxide etchant (6:1; Sigma-Aldrich) for 30 seconds and rinsed into deionized (DI) water for 5 minutes. Thereafter, subsequent thermal annealing was conducted at 900°C by using pulsed-laser deposition for 90 minutes. We grew the $Sr_3Al_2O_6$ (SAO) water-soluble sacrificial layer by using a KrF excimer laser (248 nm, COMPex 205F, Coherent) at 780°C for 40 min. The laser power and frequency are 2 W and 2 Hz, respectively. Afterward, single-crystalline BTO with a thickness of 30 nm was grown on the SAO surface at 100 mTorr. The laser power and frequency are 2 W and 10 Hz, respectively. Due to the small lattice mismatch (less than 0.5%), single-crystalline BTO could be grown with a smooth surface and narrow full width at half maximum of X-ray diffraction (XRD) (Fig. S1–S3), demonstrating low defect density. Moreover, we observed the high capacitance (Fig. S4) and dielectric constant (Fig. S4 and S14) in our single-crystalline BTO, demonstrating the possibility of a high polarization density.

Synthesis of MoS_2

We used customized hot-wall asymmetric three-zone metal-organic chemical vapor deposition (MOCVD) system to synthesize monolayer MoS_2 continuous films. After cleaning with acetone, isopropanol, and deionized water, thermally grown 300-nm-thick SiO_2 on 4-inch Si wafer was placed in a quartz tube. 60 mg of Molybdenum hexacarbonyl (MHC, Sigma Aldrich, purity ≥ 99.9%) and 12.5 mL of dimethyl sulfide anhydrous (DMS, Sigma Aldrich, purity ≥ 99.0%) were used as precursors for Mo and S respectively and introduced into the quartz tube using 5.0 sccm for H_2 and 310 sccm for Ar as carrier gases. The amounts of precursors injected into chamber are precisely controlled with mass flow controllers (MFCs), with NaCl plates placed in front of the substrate where the upstream of the furnace. The optimized conditions for synthesizing the continuous films for monolayer MoS_2 included pressure of 12.5 Torr, growth temperature of 580 °C, growth time of 23 hours, MHC flow of 1.0 sccm, and DMS flow of 0.6 sccm with optimized the reacting zone positions.

Synthesis of *h*-BN

The growth of *h*-BN was performed in a metal-organic vapor phase epitaxy (Aixtron) close-coupled showerhead (CCS) reactor on the 2-inch sapphire substrate at 1280 °C and 90 mbar pressure. Triethylboron (TEB) and ammonia (NH_3) were used as B and N precursors, respectively. The hydrogen was used as carrier gas. The growth rate is 15 nm/hour.

Characterization

To evaluate the structural performance of as-grown BTO, an environmental scanning electron microscopy (SEM) measurement was conducted with a Thermo Fisher Scientific Quottro, operated at an accelerating voltage 10 kV. XRD and atomic force microscopy (AFM) measurements were conducted to measure the 3D material quality. XRD rocking curves of the samples were obtained using a Rigaku D-Max-B with Cu K_α radiation. The AFM images were obtained using a VEECO Nanoscope IIIA AFM. Transmission electron microscopy (TEM) using a Thermo Fisher Scientific Themis Z at 200kV was used to investigate the crystallinity and record integrated differential phase contrast (iDPC) data from the BTO and 2D/3D/2D heterostructures.

For analysis of the electrical performance, we fabricated capacitor structures using the C-BTO, 2D/ C-BTO/2D, 3D/ C-BTO/3D with chemically bonded interfaces, and 3D/ C-BTO/3D without chemically bonded interface, using symmetric 30 nm Au top and bottom electrodes with a width of 5 μm. These electrodes were formed using conventional photolithography with LOR10B resist, S1805 positive photoresist, developer 319 and remover PG with the fabrication processes described in Figs. S4, S6, and S7. Frequency-dependent dielectric constant measurements were performed using a potentiostat (Biologic, SP-300). Polarization versus *vs.* electric field loops were measured at a frequency of 10 kHz using a high-voltage dielectric & ferroelectric test system (PolyK) with a probe station.

Density-functional theory calculations

Density-functional theory (DFT) calculations were performed using the Vienna Ab initio Simulation Package (VASP) (*50, 51*). We used projector augmented wave (PAW) potentials and the spin-polarized generalized gradient approximation (GGA) within the Perdew-Burke-Ernzerhof (PBE) functional for the exchange-correlation energy (*52, 53*). The PAW potentials explicitly included the valence electrons as follows: $5d^{10}6s^1$ for Au, $4p^64d^55s^1$ for Mo, $3s^23p^4$ for S, $5s^25p^66s^2$

for Ba, $3p^6 3d^2 4s^2$ for Ti, $2s^2 2p^4$ for O, respectively. The plane-wave cutoff energy was set to 600 eV. The Brillouin zone was sampled with Γ-centered 4×1×1 k-point meshes. To obtain more accurate layer spacing in the slab models, we employed the Grimme-D3 dispersion correction (*54*), as implemented in the VASP. In addition, dipole correction with a large vacuum thickness (~20 Å) along the *c*-axis was employed in the slab calculations to remove any fictitious dipole interactions between the periodic images. The convergence criteria were set to 10^{-7} eV for energy and 0.01 eV/Å^2 for forces, respectively.

Using this approach, we constructed a sandwich-type heterostructure ('Au/MoS_2/BTO/MoS_2/Au'), consisting of the following materials: $\sqrt{3} \times 7 \times 1$ supercell of 2*H*-MoS_2, $\sqrt{2} \times 4\sqrt{2} \times 1$ supercell of *P*4*mm*-BTO (001), and $\sqrt{2} \times 4\sqrt{2} \times 1$ supercell of Au (001), respectively. This gives less than 1% of lattice mismatch for BTO and MoS_2 layers along the *ab*-plane. To find the optimal lattice spacing between MoS_2 and ferroelectric BTO layers, we kept the atomic positions of the BTO at its bulk configuration of tetragonal phase (*P*4*mm*), and the MoS_2 layers were fully relaxed using the conjugated gradient algorithm. We fixed the interlayer distance between Au and MoS_2 as 3 Å, which is comparable to other reported metal-MoS_2 contact distances (*55*).

Weibull distribution analysis

The dielectric breakdown behavior of the samples was statistically analyzed with a two-parameter Weibull distribution function:

$$P(E_i) = 1 - \mathrm{e}^{-(\frac{E_i}{E_b})^{\beta}}$$

Here E_i is the measured breakdown field, $P(E_i)$ is the cumulative probability of electric breakdown at E_i, E_b is the statistical breakdown strength at which $P(E_i)$ equals 63.2%, and the Weibull parameter β evaluates the distribution of E_i. Ten different samples were investigated for each composition for the analysis.

Supplementary Text

Miller model

The Miller model can be derived from the classical damping theory for ferroelectric capacitors (*56*). From the damping theory, the damping response of the spontaneous polarization can be effectively modeled by Debye's dielectric relaxation model (*57*). Due to the lagging response of the spontaneous dipole moment, the rate at which the dipole moment change is as follows:

$$\frac{dp_s}{dt} = -\frac{p_s - \alpha_f(0)E(t)}{\tau} \tag{S1}$$

Here, p_s is an instantaneous spontaneous dipole moment, $\alpha_f(0)$ is the direct current (DC) polarizability for spontaneous polarization in ferroelectric materials, $E(t)$ is an external electric field, and τ is the relaxation time of the dipole. For an alternating current (AC) condition, the external field can be expressed by an exponential representation as follows:

$$E(t) = E_0 \exp(j\omega\tau) \tag{S2}$$

Here E_0 is the amplitude of the field, j is an imaginary number, and ω is the angular frequency of the AC condition. If the field is substituted into Equation (S1.1), an ordinary differential equation that describes the lagging response is obtained as follows:

$$\frac{dp_s}{dt} = -\frac{p_s}{\tau} + \frac{\alpha_f(0)}{\tau} E_0 \exp(j\omega\tau) \tag{S3}$$

Solving the differential equation for the p_s, the Equation (S3) is expressed as follows:

$$p_s = \alpha_f(\omega) E_0 \exp(j\omega\tau) \tag{S4}$$

where $\alpha_f(\omega)$ is the AC polarizability of the p_s, and $\alpha_f(\omega)$ can be described as follows:

$$\alpha_f(\omega) = \frac{\alpha_f(0)}{1+j\omega\tau} \quad \text{(S5)}$$

According to Equation (S5), $\alpha_f(\omega)$ at low τ is nearly equal to $\alpha_f(0)$ at a certain frequency. This result indicates that the p_s closely follows the external field. At the high τ, the τ is larger than the AC period of the field and the p_s does not follow the field. That is, the large τ suppresses the AC polarizability depending on the external AC bias, providing relatively low remnant polarization.

Maxwell-Wagner (MW) relaxation

MW relaxation (or Maxwell-Wagner-Sillars relaxation) is the phenomenon of charge accumulation at the heterogeneous interfaces of the dielectric materials with different permittivity and conductivity. This relaxation is equivalent to the charging two series capacitors when the current flows across the heterogeneous interface. The conduction current through each material is given by

$$j_1 = \sigma_1 E_1 \; and \; j_2 = \sigma_2 E_2 \quad \text{(S6)}$$

where E represents the electric field and σ is the conductivity of the two different materials. Before reaching the steady state, the conduction currents in each material are not equal. The electric field can be expressed as follows:

$$E_1 = \frac{\sigma_2}{d_1\sigma_1+d_2\sigma_2}U + \left(\frac{\varepsilon_{r2}}{d_1\varepsilon_{r2}+d_2\varepsilon_{r1}} - \frac{\sigma_2}{d_1\sigma_2+d_2\sigma_1}\right)Ue^{-\frac{t}{\tau}} \quad \text{(S7)}$$

$$E_2 = \frac{\sigma_1}{d_1\sigma_1+d_2\sigma_2}U + \left(\frac{\varepsilon_{r1}}{d_1\varepsilon_{r2}+d_2\varepsilon_{r1}} - \frac{\sigma_1}{d_1\sigma_2+d_2\sigma_1}\right)Ue^{-\frac{t}{\tau}} \quad \text{(S8)}$$

where U is the polarization voltage applied on the heterostructure, d is thickness, ε_r is the relative permittivity, and t is time.

Electronic structure of MoS_2/C-BTO/MoS_2 heterostructures

To gain a comprehensive understanding of the polarization behavior within the 2D/3D/2D heterostructures, we calculated their electronic structure using DFT. We created a series of

sandwich-type heterostructures ('Au/MoS_2/BTO/MoS_2/Au') consisting of either 1 or 2 monolayers (ML) of MoS_2, 3-unit cells-thick BTO, and 3 layers of Au as contacts (details in the 'Materials and Methods' section). Fig. S10 and S11 show the layer-projected density of states for the heterostructures with one monolayer (1ML)- and two monolayer (2ML)-MoS_2, respectively. In both cases, the intrinsic electric field within the ferroelectric BTO layers induces a potential gradient and band bending indicated by the red lines. This leads to a charge transfer, from the valence band of the top BTO layer to the conduction band of the bottom BTO layer. We note that the middle BTO layer, corresponding to the bulk region, remained insulating. These polarization-induced charges impact the adjacent MoS_2 layer, transitioning it to a metallic state, as shown in Fig. S10 and S11. However, with 2ML-MoS_2, the MoS_2 layers away from BTO (*i.e.*, in contact with the Au electrode) show only a small density of states at the Fermi energy due to transfer of electrons from the Au contact (and do not follow the trend in band shift observed in BTO), indicating that the polarization-induced charges can be screened completely by 1ML-MoS_2. These results are in excellent agreement with the experimental PE measurements wherein a significant reduction in the remnant polarization of 2ML-MoS_2/C-BTO/2ML-MoS_2 is observed.

We also investigated the laterally averaged charge density difference along the *c*-axis ($\Delta\rho$) for the heterostructures (Fig. S10 and S11), which is defined as the difference of charge density of the heterostructure ('MoS_2/BTO/Au') after subtracting the superposed charge density of two isolated systems ('MoS_2/Au' and 'BTO'). In common, the spontaneous polarization within the BTO layers results in the charge accumulation at the interface between BTO and adjacent MoS_2 layers (blue shaded area). Meanwhile, the charge transfer into the non-adjacent MoS_2 layer is negligible (orange shaded area). Consequently, the aggregated electrons and holes are confined within the adjacent MoS_2 layers to the interface, which suggests that 1 ML-MoS_2 can effectively screen the negative or positive polarization bound charges.

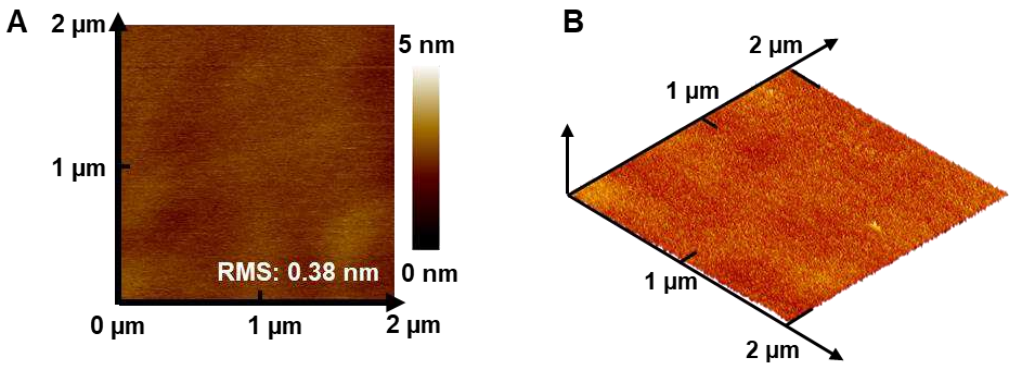

Fig. S1

Atomic-force microscopy (AFM) images of the as-grown BTO. (**A**) Plan-view and (**B**) three-dimensional AFM image of the as-grown BTO.

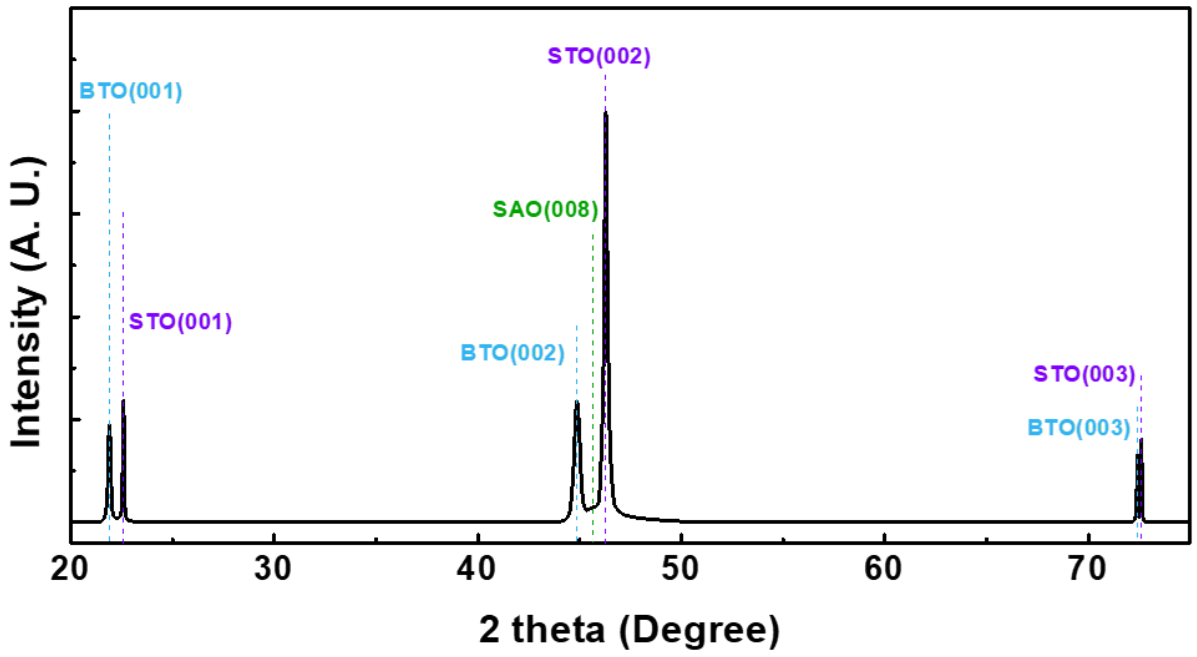

Fig. S2

XRD rocking curve of the as-grown BTO. Theta-2theta XRD rocking curve of the as-grown BTO. The full width at half maximum value of BTO was calculated to be ~0.2º.

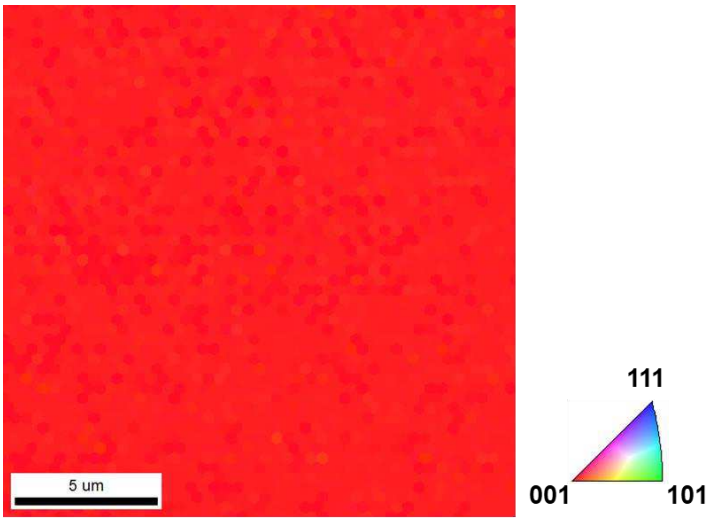

Fig. S3

Electron back-scattering diffraction (EBSD) mapping of the as-grown BTO. Plan-view EBSD mapping of the as-grown C-BTO. Only (001) plane is observed at the surface, indicating the C-BTO was grown with single-crystalline.

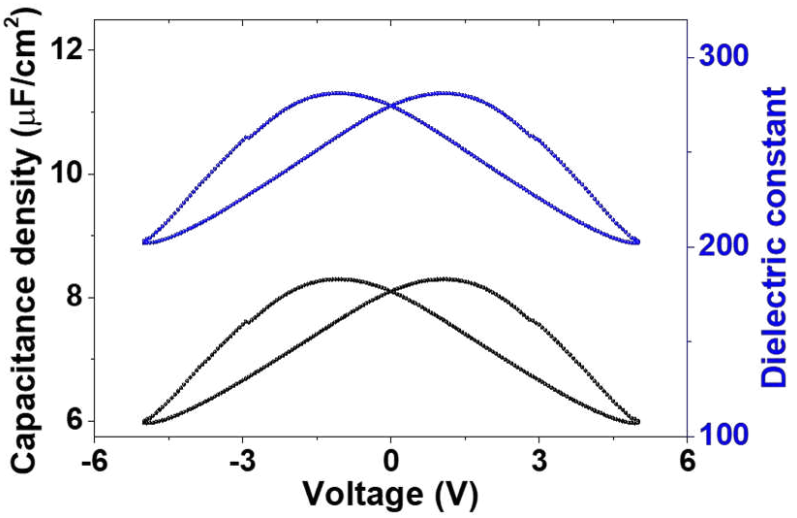

Fig. S4

Capacitance vs. voltage (CV) curve of the C-BTO. CV curve and dielectric constant calculated from capacitance of the Au/C-BTO/Au structure at 10 kHz.

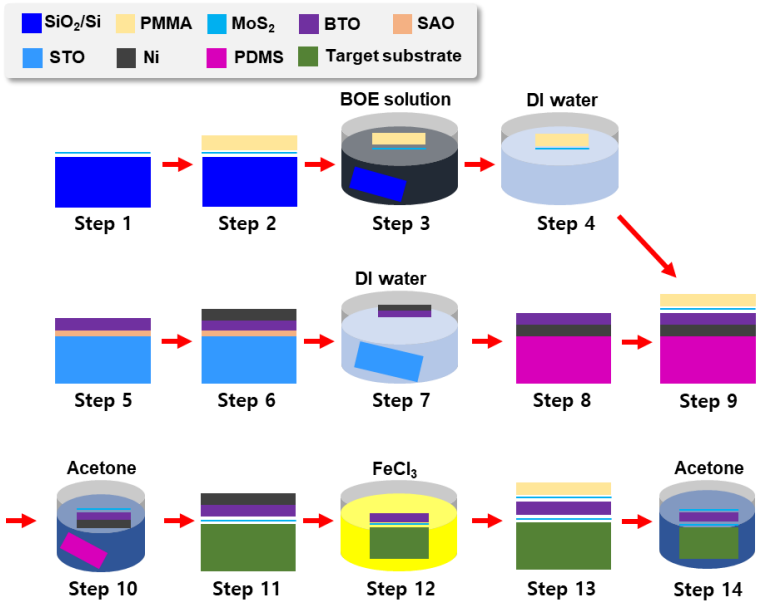

Fig. S5

2D/C-BTO/2D fabrication process. Schematic illustration of the fabrication process for 2D/C-BTO/2D structure. In this process, we used 1ML-MoS_2 as an example. (Step 1) We grew the single-domain MoS_2 onto the SiO_2/Si substrate via chemical vapor deposition. (Step 2) Poly(methyl methacrylate) (PMMA) was placed on the MoS_2 layer as a handling layer. (Step 3) SiO_2 sacrificial layer has been etched using buffered oxide etchant (BOE). (Step 4) We rinsed the PMMA/MoS_2 layer by using DI water. (Step 5) To prepare the freestanding BTO nanomembrane, we grew the BTO/SAO onto STO and (Step 6) deposited the Ni handling layer by using DC plasma for 12 minutes in physical vapor deposition (PVD). (Step 7) The sample is left to float onto DI water for 6 hours to etch the SAO sacrificial layer. (Step 8) We scooped the freestanding Ni/BTO layer onto the Polydimethylsiloxane (PDMS) and dried overnight. (Step 9) By using standard wet transfer, PMMA/MoS_2 layers were formed on the BTO surface. (Step 10) We etched the PMMA layer into acetone at 40°C for 30 minutes. The PDMS handling layer is automatically detached from Ni/BTO. (Step 11) For the 2ML-MoS_2/C-BTO/2ML-MoS_2, we repeatedly performed steps 2 to 4, then employed the layer transfer method (*12, 15, 26*) to transfer another PMMA/MoS_2 layer onto the MoS_2/BTO/Ni/PDMA surface. We scooped the freestanding Ni/BTO/MoS_2 layer onto the target substrate and dried overnight. (Step 12). To etch the Ni handling layer, we dipped the sample into $FeCl_3$ solution for 1 minute. (Step 13) For the 2D/C-BTO/2D sandwich structure, we transferred the PMMA/MoS_2 layer onto the BTO surface. (Step 14) PMMA layer has been etched as in Step 10.

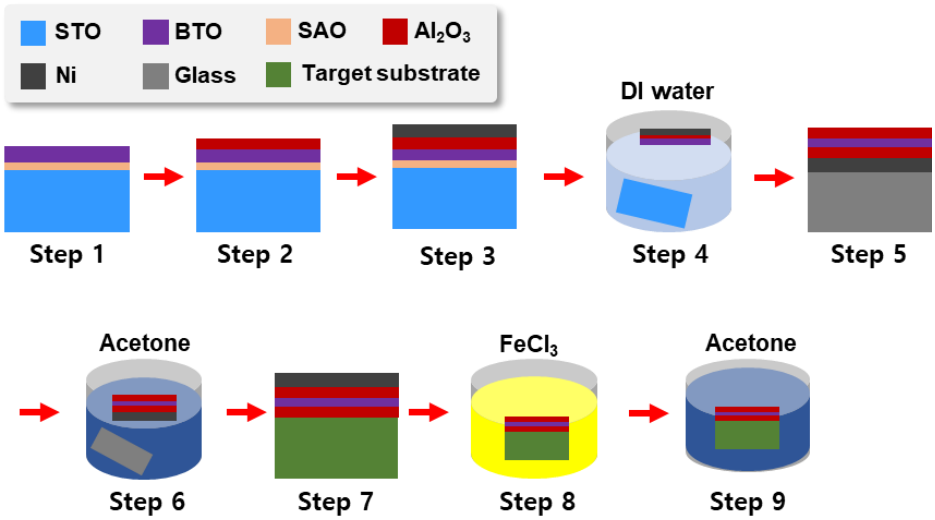

Fig. S6

Strongly chemically-bonded 3D/C-BTO/3D fabrication process. (**A**) Schematic illustration of the fabrication process for 3D/C-BTO/3D structure with a strongly chemically bonded interface. (Step 1) To prepare the freestanding BTO nanomembrane, we grew the BTO/SAO onto STO and (Step 2) deposited the 3-nm thick Al_2O_3 by using atomic layer deposition (ALD) to form the chemical bonded interface (*58*). (Step 3) Ni handling layer was deposited using DC plasma for 12 minutes in PVD. (Step 4) The sample has been left to float onto DI water for 6 hours to etch the SAO sacrificial layer. (Step 5) We scooped the freestanding Ni/Al_2O_3/BTO layer onto the cover glass and dried overnight. Thereafter, we deposited the Al_2O_3 with a thickness of 3 nm using ALD at 175ºC. (Step 6) We exfoliated the Al_2O_3/BTO/Al_2O_3/Ni layer from the glass into acetone. (Step 7) We scooped the freestanding layer onto the target substrate and dried overnight. (Step 8) To etch the Ni handling layer, we dipped the sample into $FeCl_3$ solution for 1 minute. (Step 9) For cleaning, we rinsed the sample in acetone at 40 ºC for 30 minutes.

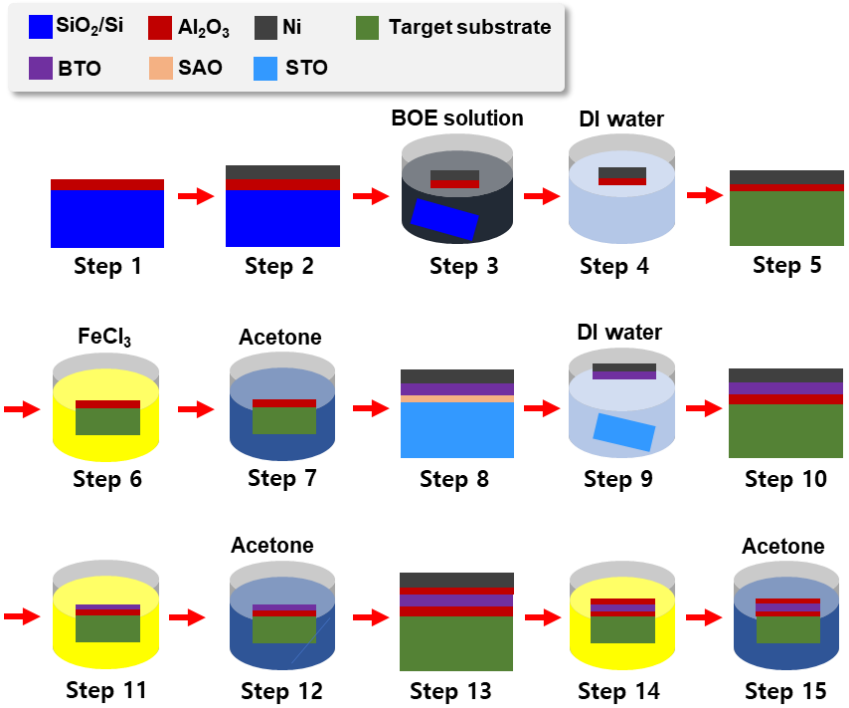

Fig. S7

Weakly bonded 3D/C-BTO/3D fabrication process. Schematic illustration of the fabrication process for 3D/C-BTO/3D structure without strong chemical bonds at the interface. (Step 1) We deposited the 3-nm thick Al_2O_3 on SiO_2/Si substrate by ALD. (Step 2) Ni handling layer was deposited using DC plasma for 12 minutes in PVD on the top of the Al_2O_3. To prepare the freestanding Al_2O_3 nanomembrane, we etched the SiO_2 layer onto BOE and (Step 4) immediately rinsed the Ni/Al_2O_3 freestanding layer in DI water. (Step 5) We transferred the freestanding layer onto the target substrate and dried it overnight. (Step 6) To etch the Ni handling layer, the sample was dipped into $FeCl_3$ solution for 1 minute. (Step 7) We rinsed the sample in acetone at 40°C for 30 minutes. (Step 8) To prepare the freestanding BTO nanomembrane, we deposited Ni on the surface of the BTO for 12 minutes. (Step 9) We etched the SAO sacrificial layer in DI water for 6 hours and (Step 10) transferred it to the surface of the Al_2O_3. (Step 11) Thereafter, we etched the Ni and (Step 12) rinse the sample. The formation process of top Al_2O_3 (Step 13 – Step 15) used the same method as the bottom Al_2O_3. (Step 5 – Step 7). During the process, we avoid any additional thermal annealing process, which would lead to stronger chemical bonds at the interface (*59, 60*).

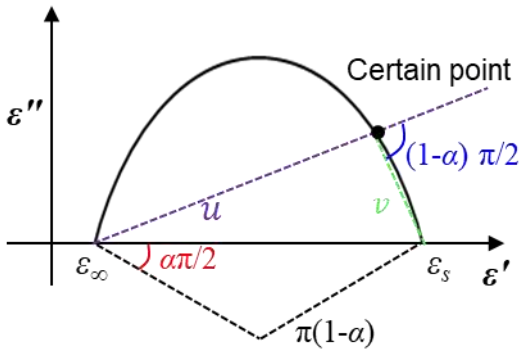

Fig. S8

Cole-Cole plot illustration. Schematic illustration of the Cole-Cole plot where the relaxation time is calculated as follows: $\frac{u}{v} = (\omega\tau)^{1-\alpha}$. u is the distance from a particular data point in the Cole-Cole plot from point ε_∞, v is the distance of the same data point from point ε_s, and α is the distribution parameter that ranges from 0 to 1. For calculations, we calculated the relaxation time at 10 kHz.

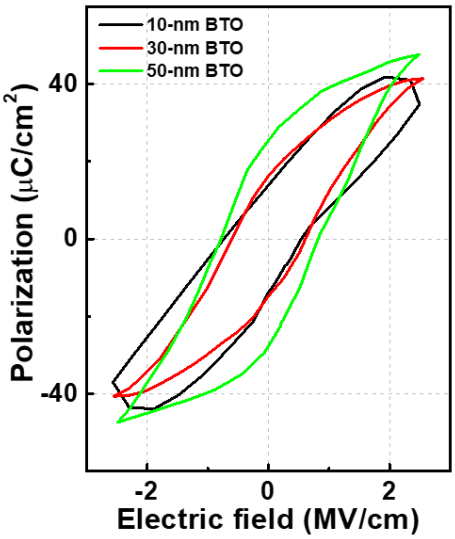

Fig. S9.

***P-E* loops of C-BTO with different thicknesses.** *P-E* loop of BTO according to the thickness. For the 10 nm C-BTO sample, a round shape indicates high electrical leakage, while 50 nm thick C-BTO exhibits substantial energy loss attributed to its large P_r. Considering these results, we selected C-BTO with a thickness of 30 nm for all other measurements.

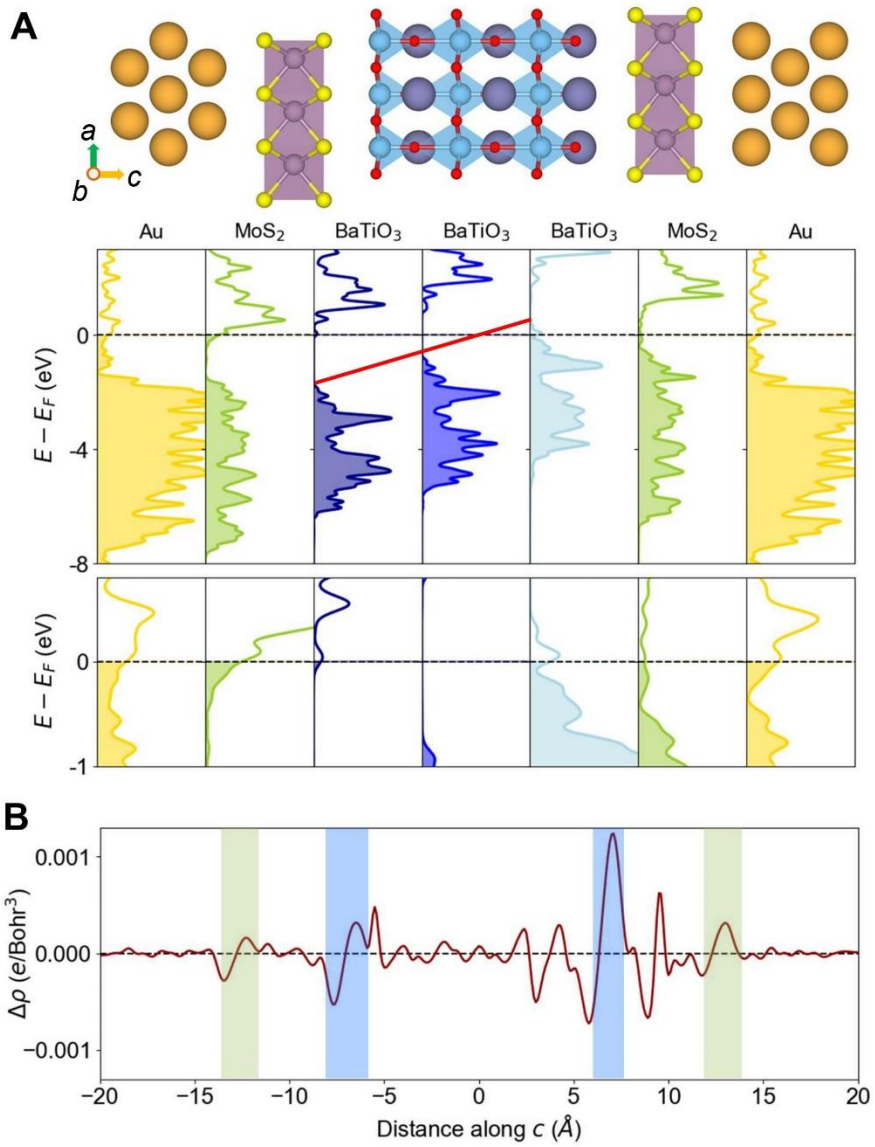

Fig. S10

Electronic structure of the 1ML-MoS_2/C-BTO/1ML-MoS_2 heterostructure from DFT. (**A**) Atomic configuration (top) and layer-projected density of states (bottom) across the 'Au/1ML-MoS_2/$BaTiO_3$/1ML-MoS_2/Au' heterostructure. Color legends: Au – orange, Mo – light purple, S – yellow, O – red, Ti – sky blue, Ba – dark blue. Red line shows the polarization-induced band bending within the $BaTiO_3$ layer. (**B**) Laterally averaged charge density difference along the *c*-axis of the 'Au/1ML-MoS_2/$BaTiO_3$/1ML-MoS_2/Au' heterostructure. The shaded blue and green areas represent the interface regions of MoS_2/$BaTiO_3$ and MoS_2/Au contacts, respectively.

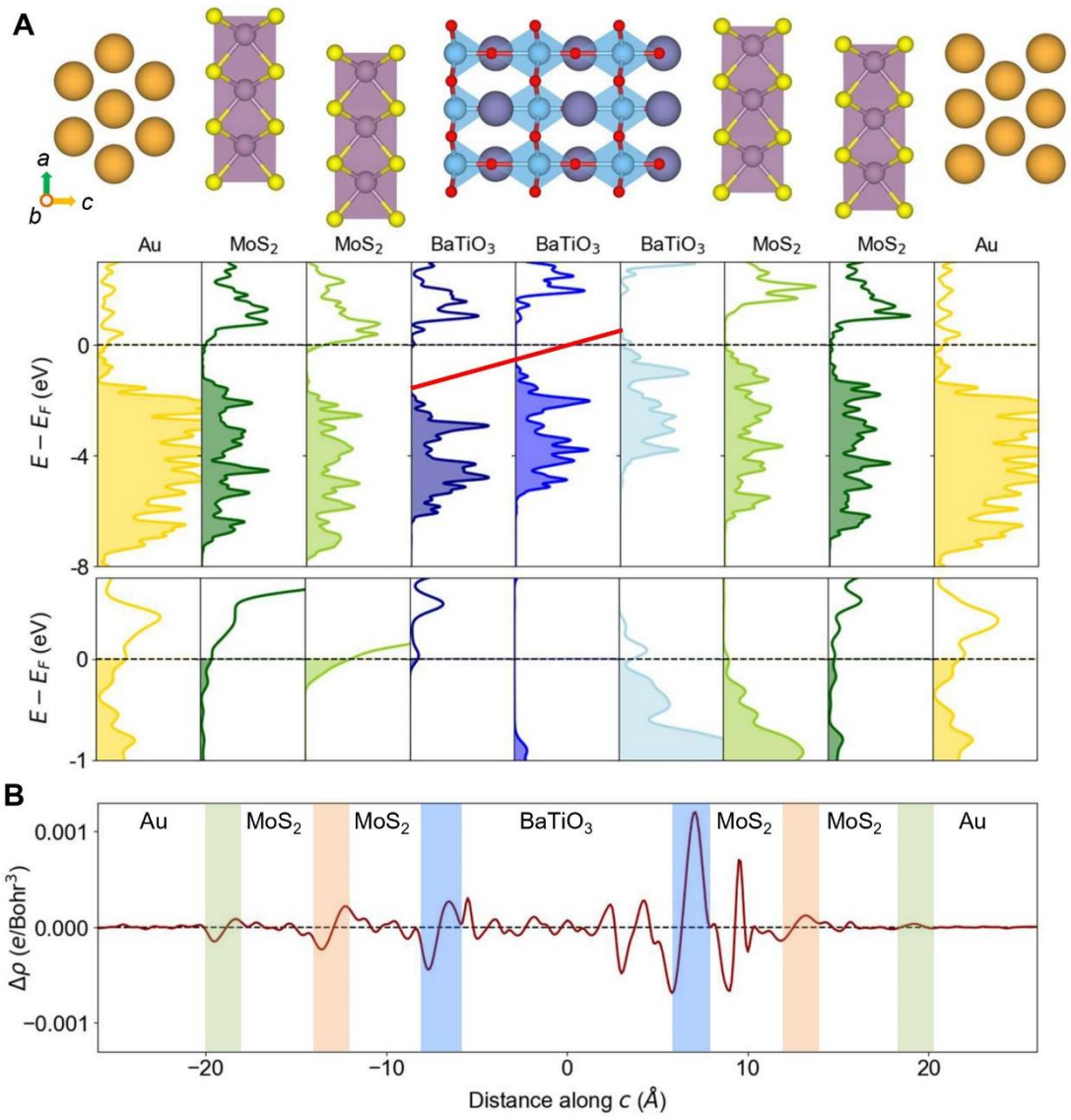

Fig. S11

Electronic structure of the 2ML-MoS_2/C-BTO/2ML-MoS_2 heterostructure. (**A**) Atomic configuration (top) and layer-projected density of states (bottom) across the 'Au/2ML-MoS_2/$BaTiO_3$/2ML-MoS_2/Au' heterostructure. Color legends: Au – orange, Mo – light purple, S – yellow, O – red, Ti – sky blue, Ba – dark blue. Red line shows the polarization-induced band bending within the $BaTiO_3$ layer. (**B**) Laterally averaged charge density difference along the *c*-axis (bottom) of the 'Au/2ML-MoS_2/$BaTiO_3$/2ML-MoS_2/Au' heterostructure. The shaded blue, orange, and green areas represent the interface regions of MoS_2/$BaTiO_3$, MoS_2/MoS_2, and MoS_2/Au contacts, respectively.

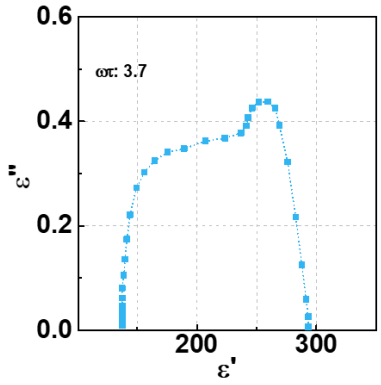

Fig. S12

Dielectric Cole-Cole plot. Dielectric Cole-Cole plots of the of the 2ML-MoS_2/C-BTO/2ML-MoS_2 over the frequency range from 10^2 to 10^6. The $\omega\tau$ and relaxation time are calculated to be 3.7 and 59.5 μs.

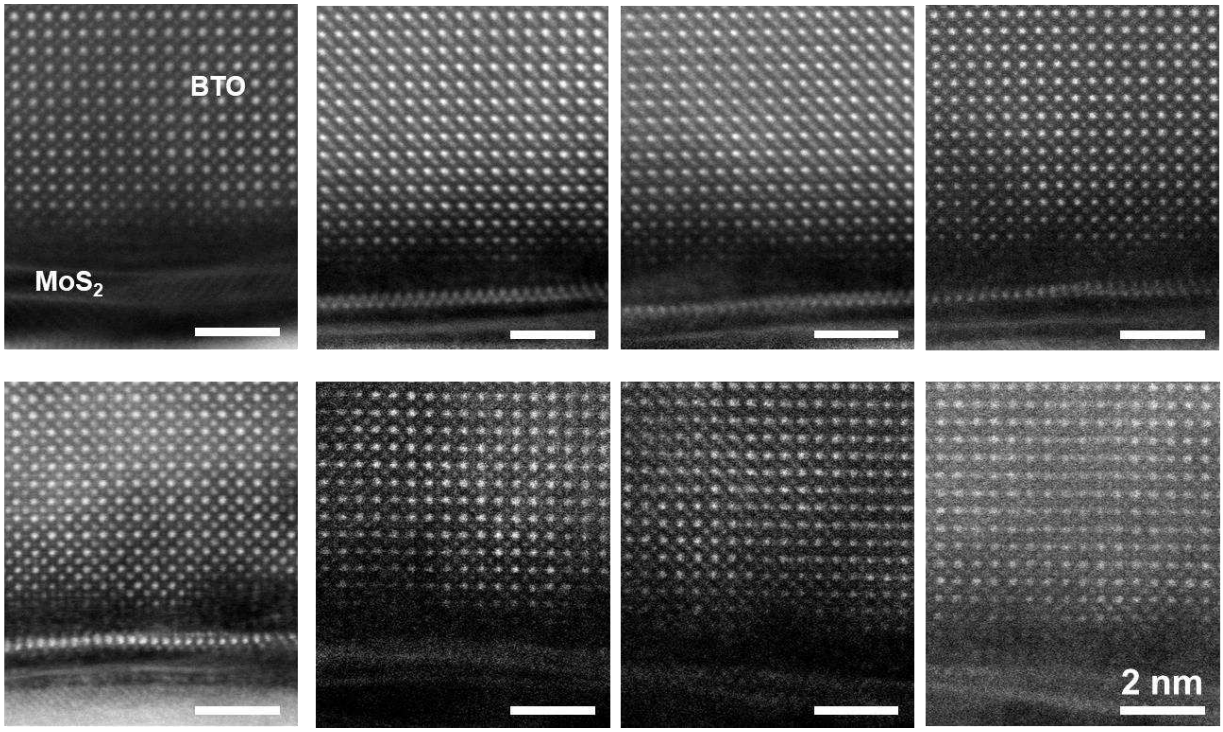

Fig. S13

High-angle annular dark field (HAADF) images of the 2ML-MoS_2/C-BTO/2ML-MoS_2. HAADF images of the 2ML-MoS_2/C-BTO/2ML-MoS_2 obtained from several different regions of the sample. The average gap between BTO and MoS_2 in the images is calculated to be 0.8 +/- 0.08 nm with a standard deviation of 0.45 in nine samples. This variability is related to the roughness visible at the BTO surface.

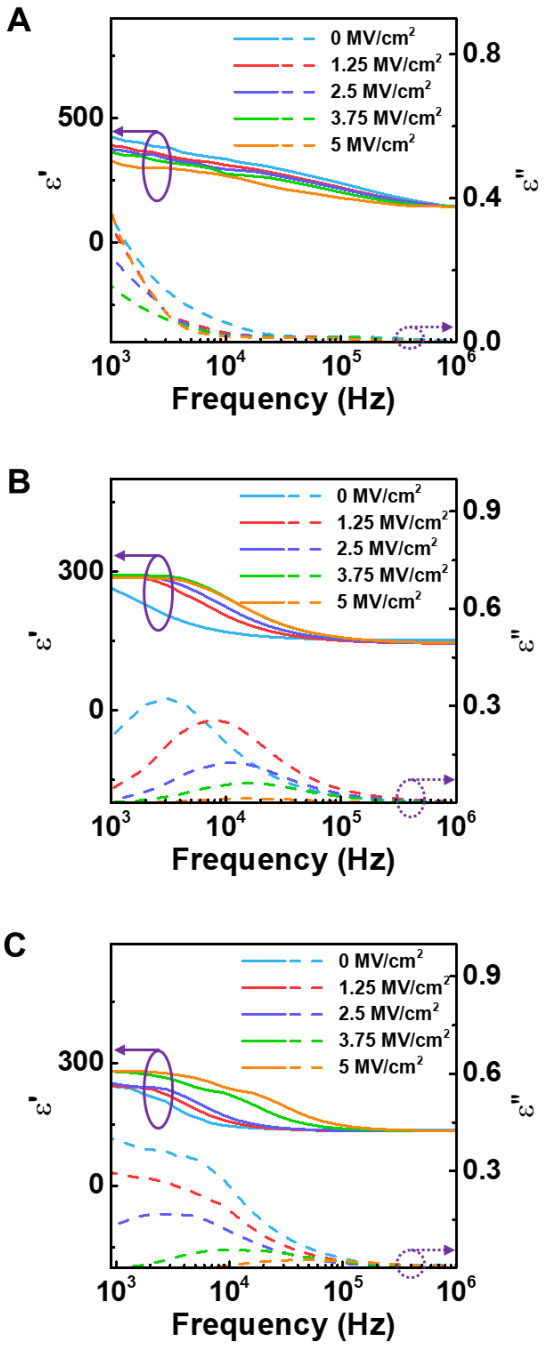

Fig. S14

Frequency dependent dielectric constant curves. Frequency dependent real dielectric constant and imaginary dielectric constant curves of the (**A**) C-BTO, (**B**) 1ML-MoS_2/C-BTO/1ML-MoS_2, and (**C**) 2ML-MoS_2/C-BTO/2ML-MoS_2. Gaussian curves in 1ML-MoS_2/C-BTO/1ML-MoS_2 and 2ML-MoS_2/C-BTO/2ML-MoS_2 are shifted with increasing the DC electric field, indicating the point shift in dielectric Cole-Cole plots.

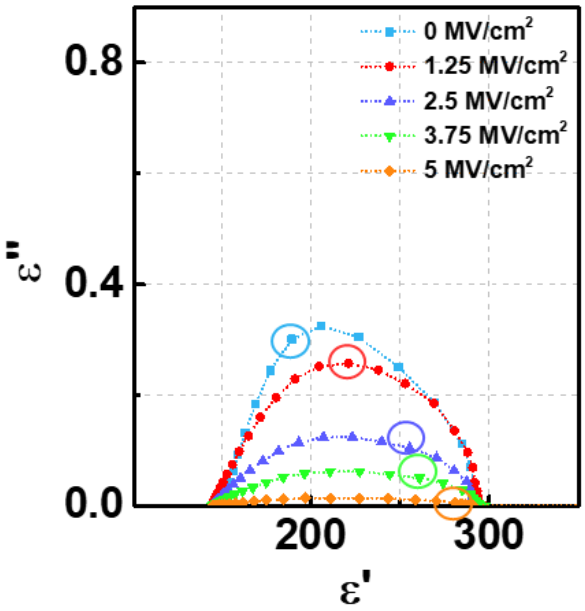

Fig. S15

DC electric field dependent Cole-Cole plot. Dielectric Cole-Cole plot of the MoS_2/C-BTO/MoS_2 with respect to the DC electric field at the AC field of 100 mV at 10 kHz.

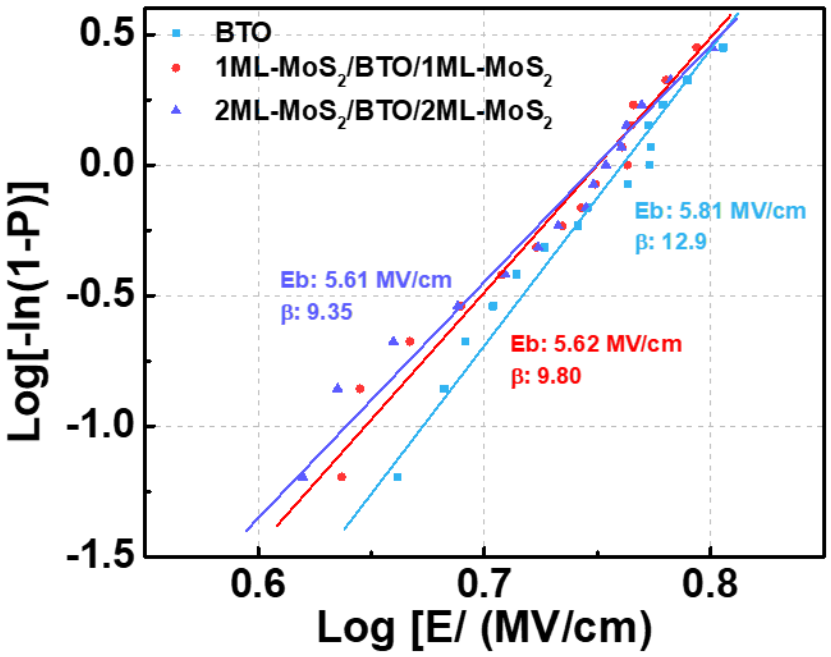

Fig. S16

Two-parameter Weibull distribution analysis of breakdown strengths. Two-parameter Weibull distribution analysis of breakdown strengths of the C-BTO, 1ML-MoS_2/C-BTO/1ML-MoS_2, and 2ML-MoS_2/C-BTO/2ML MoS_2. Ten different samples were investigated for each composition for the analysis.

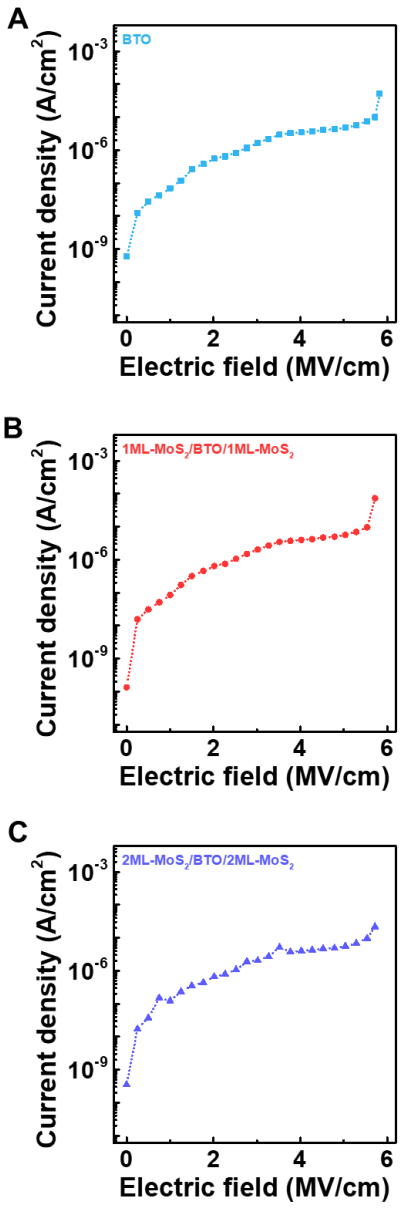

Fig. S17

Leakage current densities of the C-BTO and MoS_2/C-BTO/ MoS_2. The leakage current density *vs.* electric field is shown for (**A**) C-BTO, (**B**) 1ML-MoS_2/C-BTO/1ML-MoS_2, and (**C**) 2ML-MoS_2/C-BTO/2ML-MoS_2.

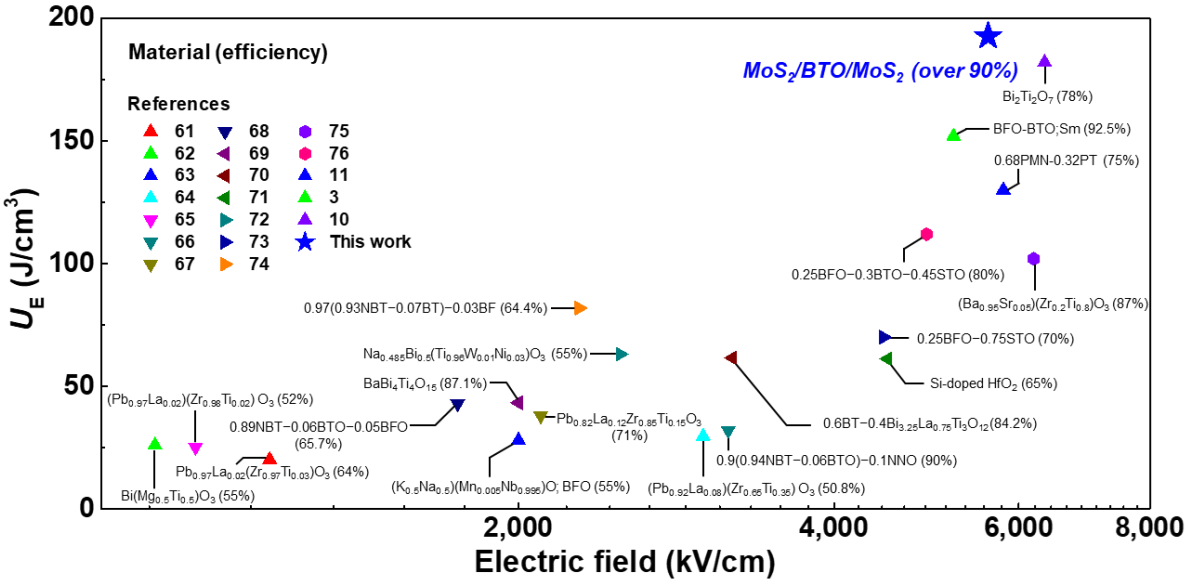

Fig. S18

Comparative energy densities of different structural configurations. Comparison of the energy densities of representative electrostatic capacitors in previous studies with the 2D/C-3D/2D heterostructure-based capacitor described here.

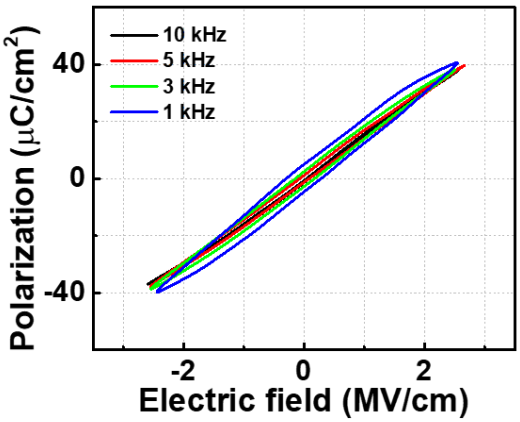

Fig. S19.

Frequency dependent energy storage performance of the 2ML-MoS_2/BTO/2ML-MoS_2. *P-E* loop of the 2ML-MoS_2/BTO/2ML-MoS_2 sample with frequencies of 10, 5, 3, and 1 kHz.

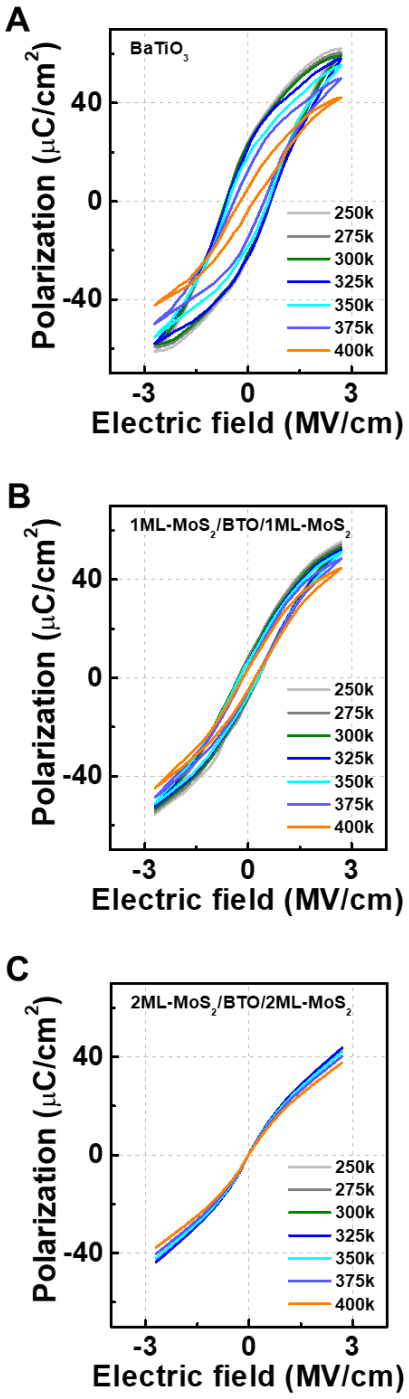

Fig. S20

Temperature-dependent *P-E* loops of the C-BTO and MoS_2/C-BTO/ MoS_2 samples. *P-E* loops of (**A**) C-BTO, (**B**) 1ML-MoS_2/C-BTO/1ML-MoS_2, and (**C**) 2ML-MoS_2/C-BTO/2ML-MoS_2 at temperatures ranging from 250 to 400K.

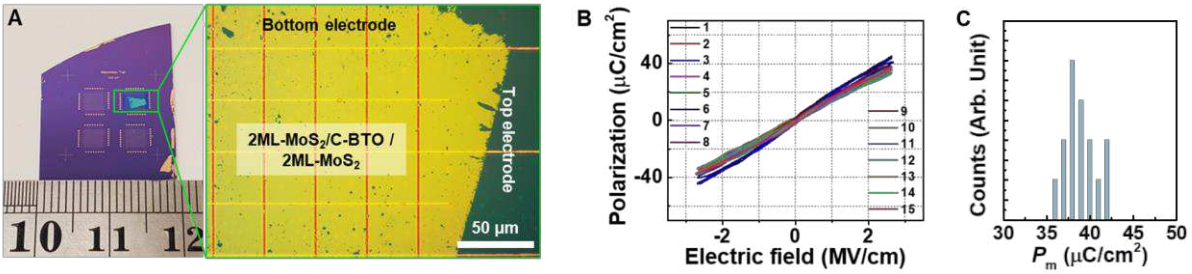

Fig. S21

2ML-MoS_2/C-BTO/2ML-MoS_2 array. (A) Photograph (left) and light microscope image (right), and (**B**) *P*-*E* loops of 2ML-MoS_2/C-BTO/2ML-MoS_2 heterostructures in an array. (**C**) P_m histogram of the 2ML-MoS_2/BTO/2ML-MoS_2 heterostructures in the array, where the P_m values are calculated rounded to the nearest whole number.

REFERENCES AND NOTES

1. J.-K. Huang *et al.*, *Nature* **605**, 262-267 (2022).
2. A. J. Yang *et al.*, *Nat. Electron.* **5**, 233-240 (2022).
3. H. Pan *et al.*, *Science* **374**, 100-104 (2021).
4. Q. Li *et al.*, *Nature* **523**, 576-579 (2015).
5. H. Luo *et al.*, *Adv. Sci.* **9**, 2202438 (2022).
6. X.-K. Wei *et al.*, *Adv. Mater.* **32**, 2003479 (2020).
7. J. P. B. Silva *et al.*, *ACS Energy Lett.* **6**, 2208-2217 (2021).
8. L. Yang *et al.*, *Prog. Mater. Sci.* **102**, 72-108 (2019).
9. T. Li *et al.*, *Adv. Funct. Mater.* **32**, 2202307 (2022).
10. B. Yang *et al.*, *Nat. Mater.* **21**, 1074-1080 (2022).
11. J. Kim *et al.*, *Science* **369**, 81-84 (2020).
12. J. Shim *et al.*, *Science* **362**, 665-670 (2018).
13. Z. Wu *et al.*, *Adv. Mater.* **34**, 2107538 (2022).
14. M. Qin, L. Zhang, H. Wu *et al.*, *Adv. Sci.* **9**, 2105553 (2022).
15. S.-H. Bae *et al.*, *PNAS* **114**, 4082-4086 (2017).
16. M. T. Sebastian, R. Ubic, H. Jantunen, *Int. Mater. Rev.* **60**, 392-412 (2015).
17. Md. T. Rahman, M. Vargas, C. V. Ramana, *J. Alloys Compd.* **617**, 547-562 (2014).
18. S. S. Cheema *et al.*, *Nature* **604**, 65-71 (2022).
19. H. W. Park *et al.*, *Adv. Funct. Mater.* **33**, 2206637 (2023).
20. Y. J. Kim *et al.*, *Sci. Rep.* **6**, 19039 (2016).
21. A. K. Saha, M. Si, P. D. Ye, S. K. Gupta., *Appl. Phys. Lett.* **119**, 122903 (2021).
22. J. P. B. Silva *et al.*, *J. Mater. Chem. A* **8**, 14171-14177 (2020).
23. Z. Wu *et al.*, *ACS Appl. Mater. Interfaces* **10**, 11108-11115 (2018).
24. J. Shin *et al.*, *Nature* **614**, 81-87 (2023).
25. H. Kim *et al.*, *Nat. Nanotechnol.* **18**, 464-470 (2023).
26. S.-H. Bae *et al.*, *Nat. Mater.* **18**, 550-560 (2019).
27. A. Laturia, W. G. Vandenberghe, in *2017 International Conference on Simulation of Semiconductor Processes and Devices (SISPAD)*. (IEEE, 2017), pp. 337-340.
28. H. Zhou, Y. Cai, G. Zhang, Y.-W. Zhang, *Nanoscale* **10**, 480-487 (2018).
29. J.-H. Ahn *et al.*, *Nano. Lett.* **15**, 3703-3708 (2015).
30. S.-I. Kim *et al.*, *Synth. Met.* **299**, 117464 (2023).
31. A. Perepeliuc *et al.*, *Appl Phys. Lett.* **122**, 263503 (2023).
32. S. Hwangbo, L, Hu, A. T. Hoang, J. Y. Choi, J.-H. Ahn, *Nat. Nanotechnol.* **17**, 500-506 (2022).
33. Y. Ahn, M. Shin, *IEEE Trans. Electron Devices* **64**, 2129-2134 (2017).
34. T. A. Hanafy, K. Elbanna, S. El-Sayed, A. Hassen, *J. Appl. Polym. Sci.* **121**, 3306-3313 (2011).
35. H. Wang, L. Yang, X. Zhang, M. H. Ang Jr., *Results Phys.* **29**, 104781 (2021).
36. B.-H. Fan *et al.*, *Compos. Sci. Technol.* **80**, 66-72 (2013).
37. K. Venkateshan, G. P. Johari, *J. Chem. Phys.* **125**, 014907 (2006).
38. M. H. Park, H. J. Kim, Y. J. Kim, T. Moon, C. S. Hwang, *Appl. Phys. Lett.* **104**, 072901 (2014).
39. M. Liu *et al.*, *ACS Appl. Mater. Interfaces* **4**, 5761-5765 (2012).
40. M. Samet *et al.*, *J. Chem. Phys.* **142**, 194703 (2015).
41. H. Hammami, M. Arous, M. Lagache, A. Kallel, *J. Alloys Compd.* **430**, 1-8 (2007).
42. Y. G. Lee *et al.*, *Appl Phys Lett* **98**, 183508 (2011).
43. T. Akamatsu *et al.*, *Science* **372**, 68-72 (2021).
44. Y. Liu, Y. Huang, X. Duan, *Nature* **567**, 323-333 (2019).
45. S. H. Kim *et al.*, *Phys. Status Solidi RRL* **13**, 1900373 (2019).

46. M. Pawlak et al., *Appl. Phys. Lett.* **101**, 042901 (2012).
47. J. Yang *et al.*, *Nat. Nanotechnol.* **7**, 91-95 (2012).
48. H. Qi *et al.*, *Adv Funct Mater* **29**, 1903877 (2019).
49. D. Li *et al.*, *Small* **19**, 2206958 (2023).
50. G. Kresse, J. Furthmüller, *Comput. Mater. Sci.* **6**, 15-50 (1996).
51. G. Kresse, . Furthmüller, *Phys. Rev. B* **54**, 11169–11186 (1996).
52. J. P. Perdew, K. Burke, M. Ernzerhof, *Phys. Rev. Lett.* **77**, 3865–3868 (1996).
53. G. Kresse, D. Joubert, *Phys. Rev. B* **59**, 1758–1775 (1999).
54. S. Grimme, J. Antony, S. Ehrlich, H. Krieg, *J. Chem. Phys.* **132**, 154104 (2010).
55. Z.-W. Zhang, *et al*., *Phys. Chem. Chem. Phys.* **25**, 9548-9558 (2023).
56. A. K. Saha, S. Datta, S. K. Gupta, *J. Appl. Phys.* **123**, 105102 (2018).
57. P. Debye, Polar Molecules, Chemical Catalog, New York (1929).
58. M. Falmbigl *et al., J. Phys. Chem. C* **121**, 16911-16920 (2017).
59. H. Wong, H. Iwai, K. Kakushima, B. L. Yang, P. K. Chu, *J. Electrochem. Soc.* **157**, G49-G52 (2010)
60. G. Evans *et al.*, *Adv. Funct. Mater.* **20**, 231-238 (2010).
61. Y. Liu, Y. Wang, X. Hao, J. Xu, *Ceram. Int.* **39**, S513−S516 (2013).
62. J. Xie *et al*., *J. Am. Ceram. Soc.* **102**, 3819-3822 (2019).
63. S. S. Won et al., *Appl. Phys. Lett.* **110**, 152901 (2017).
64. B. Sun *et al., Ceram. Int.* **45**, 20046-20050 (2019).
65. Y. Wang, X. Hao, J. Xu, *J. Mater. Res.* **27**, 1770-1775 (2012).
66. Y. Yao *et al., J. Alloys Compd.* **750**, 228-234 (2018).
67. Y. Zhao, X. Hao, Q. Zhang, *ACS Appl. Mater. Interfaces* **6**, 11633-11639 (2014).
68. Z. Tang et al., *J. Alloys Compd.* **727**, 169-176 (2018).
69. P. D. Song et al., *J. Appl. Phys.* **125**, 134101 (2019).
70. B. B. Yang et al., *Appl. Phys. Lett.* **113**, 183902 (2018).
71. F. Ali et al., *J. Appl. Phys.* **122**, 144105 (2017).
72. C. H. Yang, Q. Yao, J. Qian, Y. J. Han, J. Chen, *Ceram. Int.* **44**, 9152-9158 (2018).
73. H. Pan et al., *Nat. Commun.* **9**, 1813 (2018).
74. C. Yang et al., *Adv. Energy Mater.* **9**, 1803949 (2019).
75. K. Wang et al., *Adv. Energy Mater.* **10**, 2001778 (2020).
76. H. Pan et al., *Science* **365**, 578-582 (2019).

ACKNOWLEDGMENTS

Funding: S.-H.B. thanks support from the Institute of Materials Science and Engineering (IMSE), Washington University in Saint Louis. S.-H.B. acknowledges the financial support from the National Science Foundation (Grant No. 2240995). S.-H.B. also acknowledges that this work was partially supported by Samsung Electronics Co., Ltd. (IO221219-04250-01). D.-H.K. thanks support from Korea Institute for Advancement of Technology (KIAT) grant funded by the Korea Government (MOTIE) (P0017305, Human Resource Development Program for Industrial Innovation (Global)). J.H.A was supported by the National Research Foundation of Korea (2015R1A3A2066337). A.O acknowledges financial support from Georgia Tech Europe in Metz-France. R.M. were supported by an ARO MURI with award number W911NF-21-1-0327 and NSF through DMR-2122070 and DMR-2145797. This work used computational resources through allocation DMR160007 from the Advanced Cyberinfrastructure Coordination Ecosystem: Services & Support (ACCESS) program, which is supported by NSF. This work was carried out in part through the use of MIT.nano's facilities. E.P. acknowledges funding from MathWorks fellowship.

Author contributions: S.-H.B., S.H., and J.S.K. conceived this study. J.S.K., E.P., Y.M., Z.X, I.R, S.O.K., and Y.L. fabricated the samples and performed the experiment, with the supervision of S.-H.B. and S.H. S.L, X.Z., and B.-I.P. performed the structural performance of samples, with the supervision of J.K. J.-Y.M., S.-I.K., H.S., A.T.H., S.S., P.V., A.O., J.-H.L., and J.-H.A. prepared the 2D materials. G.Y.J. reviewed the theory about dielectric relaxation with the supervision of R.M. E.P., A.C.F., and K.R. performed the STEM and DPC characterization with the supervision of F.M.R. S.S. and J.-H.P. analyzed the 2D/3D and 3D/3D interfaces. S.B., C.K., J.Z., C.W., J.K. and D.-H.K. performed the electrical measurement. J.H., H.C., and H.-S.K. conducted the breakdown performance. S.-H.B. and S.H. wrote the first draft of the manuscript. All authors discussed the results and revised the manuscript.

Competing interests: The authors declare no competing interests or patents.

Data and materials availability: All data are available in the main text or the supplementary materials.

SUPPLEMENTARY MATERIALS

science.sciencemag.org/content/00000
Materials and Methods
Supplementary Text
Figs. S1 to S21
References (50 – 76)